Ion–Neutral Collision Modeling Using Classical Scattering With Spin-Orbit Free Interaction Potential

Samuel J. Araki and Richard E. Wirz

Abstract—A particle-in-cell Monte Carlo collision model is developed to explore dominant collisional effects on high-velocity xenon ions incident to a quiescent xenon gas at low neutral pressures. The range of neutral pressure and collisionality examined are applicable for electric propulsion as well as plasma processing devices; therefore, the computational technique described herein can be applied to more complex simulations of those devices. Momentum and resonant charge-exchange collisions between ions and background neutrals are implemented using two different models, classical scattering with spin-orbit free potential and variable-hard-sphere model, depending on the incident particle energy. The primary and charge-exchange ions are tracked separately, and their trajectories within a well-defined "Test Cell" domain are determined. Predicted electrode currents as a function of the Test Cell pressure are compared with electrode currents measured in an ion gun experiment. The simulation results agree well with the experiment up to a Test Cell pressure corresponding to a mean free path of the Test Cell length and then start to deviate with increasing collisionality at higher pressures. This discrepancy at higher pressures is likely due to the increasing influence of secondary electrons emitted from electrodes due to the high-velocity impacts of heavy species (i.e., beam ions and fast neutrals created by charge-exchange interaction) at the electrode surfaces.

Index Terms—Monte Carlo methods, particle collisions, particle scattering, particle tracking, plasma engines, simulation.

I. INTRODUCTION

IN PLASMA devices, different types of ion–atom collisions are possible, including momentum-exchange, resonant and nonresonant charge-exchange, ionization, excitation, superelastic, and radiative collisions [1]. Of these types of interactions, momentum- and charge-exchange collisions are the most important ion–atom collisional mechanisms in electric propulsion and plasma processing applications [2]. Proper modeling of these collisions is required for accurate and predictive modeling of the life and performance of these devices. For example, in the plumes of ion thrusters and Hall-effect thrusters, ions experiencing either of the two collisions are responsible for the ion population found at angles greater than the main beam divergence that can lead to impingement on spacecraft surfaces

[3]. Charge-exchange ions created in the plume can also cause the erosion of critical thruster components and can be the primary determinant of thruster life and long duration performance [3]–[6].

In an elastic collision, the particle velocities of the collision pair are altered as the energy is transfered between the particles, while the total energy and momentum of the collision pair are conserved. Resonant charge-exchange collision is similar to the elastic collision except that one or more electrons are exchanged between the collision pair. Therefore, the charge-exchange collision can be considered to be a subset of elastic collisions [7]. In order to differentiate the two processes, we call the elastic collisions without and with exchanges of an electron MEX and CEX collisions, respectively. The two collisional mechanisms have been implemented in many computational models. For example, Oh [8] developed a particle-in-cell (PIC) model for a Hall thruster plume and used a variable hard sphere (VHS) collision method for ion–neutral elastic collisions. In his model, the CEX collisions were simulated by simply switching the velocity vectors of the ion and neutral collision partners. The CEX collision has also been implemented in ion optics codes (CEX2D and CEX3D) to predict the erosion rate of the ion thruster accelerator grid caused by CEX ions impacting the grids [4]–[6]. Mikellides *et al.* [3] applied differential cross sections computed classically for ion–neutral collisions to an electrostatic thruster plume model using a Lagrangian fluid model and obtained good agreement between the computational and experimental results for the angular dependence of ion energy and flux. Giuliano and Boyd [9], [10] developed a hybrid DSMC-PIC model and used a curve-fit representative of a differential cross section to perform calculations of postcollision particle velocities.

The objective of this investigation is to develop a PIC Monte Carlo collision (PIC-MCC) model that may be used to explore the collisions between xenon ions and atoms at relatively low neutral pressures. The neutral pressure of interest is applicable for electric propulsion as well as plasma processing devices; therefore, the computational technique described herein can be applied to more complex simulations of those devices. The computational model employs a domain and boundary condition that matches the well-defined "Test Cell" experimental domain as shown in Fig. 1 and described in [11] and [12]. Using matching domains allows direct comparisons between computational and experimental results. In the experiment [11], [12], a monoenergetic xenon ion beam of 1500 eV is guided to enter a cylindrical Test Cell, and the currents on the four different electrodes (Inner Cylinder, Exit Plate, Back Aperture, and Collector Plate) are measured. The computational
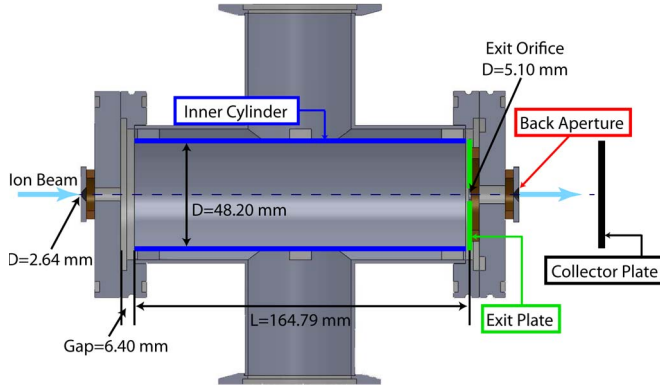
Fig. 1. Schematic of the ion beam experiment (not to scale) [11], [12]. The Back Aperture plate and the Collector Plate are placed approximately 20 and 220 mm from the Exit Plate, respectively.

results are compared with these experimental results in order to validate the model. The computational model is designed for shorter run times compared to the high-fidelity model by Giuliano and Boyd [9], [10] so that it can be used as a tool for preliminary computational analyses for the improvement and development of the experiment. This paper is organized as follows. The detailed description of the computational model is provided in Section II. An analytical model to predict the sum of the Collector Plate current and the Back Aperture current is given in Section III. Results comparing the computed and measured electrode currents are presented and discussed in Section IV. This paper closes with conclusions and future work in Section V.

II. COMPUTATIONAL MODEL DESCRIPTION

In plasma simulations, three types of computational models are often employed: a kinetic model, a fluid model, and a hybrid model in which one species is solved via fluid equations and the other species is solved by a kinetic model. At very low neutral pressure of interest, the mean free path of the ions becomes comparable to or larger than the length of the Test Cell so that the effective Knudsen (Kn) number becomes of the order of unity or greater. In this regime, the continuum assumption in the fluid equation is violated [13] so that it becomes necessary to use a kinetic model to solve the problem. For this reason, a PIC-MCC method is employed in this computational model. A high energy ion beam of 1500 eV (primary ions) is assumed to enter the cylindrical Test Cell with a uniform beam profile and without divergence. The beam radius used in the simulation is 1.32 mm, which is about 20 times smaller than the Test Cell radius. Thermal background neutrals of 300 K are assumed in the postcollision velocity calculation. In order to resolve the beam, finer grid size in this region is used with stretching grid size in the radial direction, as shown in Fig. 2.

When no xenon neutral is present in the Test Cell, all primary ions reach the Collector Plate for the case of zero beam divergence. However, as the background neutral pressure is increased, the probability of the primary ions colliding with neutrals increases, and a fraction of the ions experience elastic collisions with neutrals. As a result, the primary ions are
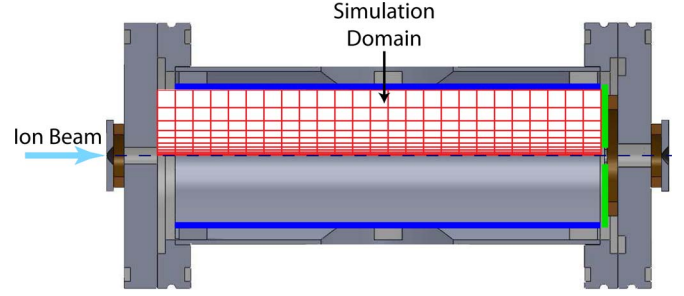

Fig. 2. Two-dimensional axisymmetric computational domain with a radially stretched grid to simulate the cylindrical "Test Cell" used in [11] and [12]. The actual grid used in the simulation is four times the resolution of the one shown in the figure.
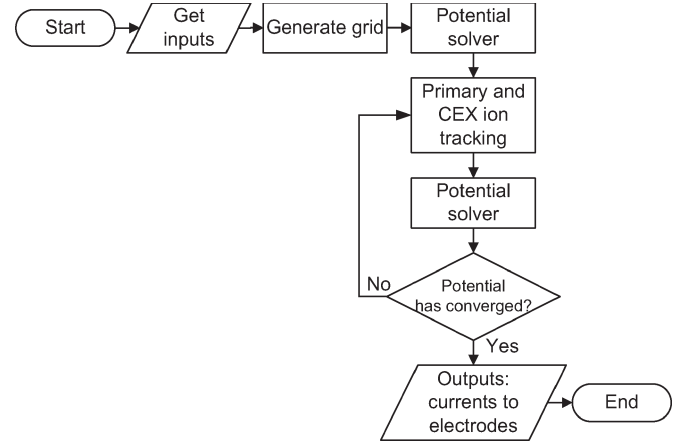

Fig. 3. Simplified flowchart for the computational model.

deflected at some angles; the scattered primary ions are called MEX ions. During the elastic collisions, the ions can gain electrons from neutrals which most commonly results in slow CEX ions and fast neutrals. Short-range Coulomb collisions between ions are less important compared to the two primary types of collisions for the range of ionization levels found in the experiment ($< 10^{-5}\%$), while long-range Coulomb interactions are incorporated in the form of electric forces calculated from space charges in the domain.

Macroparticles, each representing a fraction of the primary or CEX ion current, are tracked individually using the leap-frog method [14]. In order to find densities for all the species, particles are distributed to computational nodes at every time step using the density-conserving shape function given by Ruyten [15]. Electric potential is calculated by solving Poisson's equation with a finite difference formulation, using space charge distribution computed from particle tracking. The potential solver and particle tracking are run multiple times until the electric potential reaches steady state. Finally, computed electrode currents as a result of particles impacting the walls are determined and compared with experimental results. A simplified structure of the code is shown in Fig. 3.

A. Collision Dynamics

The elastic collisions between ions and neutrals are approximated by using two different collision models, depending on

the projectile ion energy. At energies greater than 30 eV, we use a classical scattering model with recently calculated spin-orbit free interaction potential [16], [17]. Below energies of 30 eV, the attractive force becomes dominant, and a rainbow singularity is observed in the differential cross section; thus, the VHS model [18] is employed. Most of the calculations for the collisions between the primary ions and the background neutrals are done with the classical scattering model since the primary ion energy rarely becomes less than 30 eV even after several collisions. In contrast, the CEX ions have relatively low initial energy, and their energy approaches thermal energy after multiple collisions with background neutrals; thus, the VHS model is employed in most of the collision calculations between the CEX ions and the background neutrals. For collisions between the CEX ions and the background neutrals, the difference in the collision model used does not significantly affect the result because of the large aspect ratio of the Test Cell. In other words, most of the CEX ions impact the long Inner Cylinder wall instead of the Exit Plate no matter which collision model is used.

Miller *et al.* [19] conducted a guided-ion beam experiment to find $Xe^+ + Xe$ symmetric CEX cross sections as a function of laboratory (LAB)-frame ion energy. They provided a functional form of the CEX cross section, σ_{CEX}, in square angstroms as

$$\sigma_{CEX} = 87.3 - 13.6\log(E) \tag{1}$$

where E is the LAB primary ion energy in electronvolts. At an ion energy of 1500 eV, the CEX cross section is 44.1 Å^2. Several computational models [20], [21] approximate the elastic collision cross section to be equal to the CEX cross section, i.e., $\sigma_i = \sigma_{el} + \sigma_{CEX} \approx 2\sigma_{CEX}$ where σ_i is the total ion–neutral collision cross section. Instead of using the same approximation, we use the following functional form for σ_i in square angstroms:

$$\sigma_i = 300.34 - 44.54\log(E). \tag{2}$$

The total ion–neutral collision cross section given in (2) represents the cross section within which the MEX and CEX collisions can take place and is calculated from the charge-exchange probability, P_{CEX}, as discussed in detail in Section II-D.

During a time step, Δt, the probability that a particle experiences either an elastic or a CEX collision is expressed as

$$P_{total} = 1 - \exp(-\Delta t\sigma_i v_i n_o). \tag{3}$$

Equation (3) gives a positive value that is always less than or equal to 1. Whether a collision event takes place is determined by comparing P_{total} with a uniformly probable number between 0 and 1 generated by the random number generator rand#. The random number is updated for every instance that it appears in different equations. If $P_{total} > $ rand#, then the particle experiences either a MEX or CEX collision. The depletion of macroion current, ΔJ_i, by the CEX collision is approximated by $\Delta J_i = P_{CEX}J_i$, and the remainder of the particles represented by $J_i = J_{i0} - \Delta J_i$ experience MEX collisions.
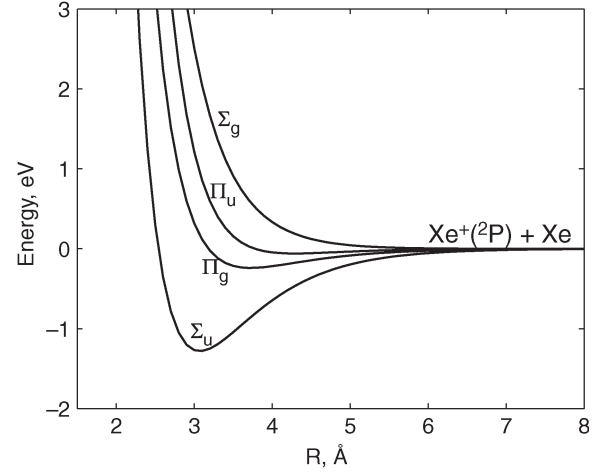

Fig. 4.   Spin-orbit free interaction potential energy curve for $Xe^+(^2P) + Xe$ calculated by Paidarova [16].

TABLE I
MORSE POTENTIAL FITTING PARAMETERS FOR AVERAGED (U, G) PAIRS OF THE SPIN-ORBIT FREE POTENTIALS (SEE [17]). VALUES ARE GIVEN IN ATOMIC UNITS (1 a.u. = 27.21 eV = 0.529 Å)

Potentials	D_e	b	r_e
$(V_{\Sigma g} + V_{\Sigma u})/2$	0.00585	0.645	7.476
$(V_{\Pi g} + V_{\Pi u})/2$	0.00487	0.677	7.570

B. $Xe^+ + Xe$ Interaction Potential

The interaction potentials for $Xe^+ + Xe$ collisions have been calculated with *ab initio* quantum chemistry [16], [22], [23]. In the computational model, four spin-orbit free potentials, Π and Σ potentials with the *gerade* (g) and the *ungerade* (u) states, calculated by Paidarova are used [16]. These potentials are shown in Fig. 4. Chiu *et al.* [17] verified that the scattering results are not affected significantly by using the full spin-orbit potentials. The averaged (u, g) pairs of the spin-orbit free potentials are fitted using the Morse potential form [17] with the fitting parameters given in Table I

$$V_{avg}(r) = D_e\left(e^{2b(r_e-r)} - 2e^{b(r_e-r)}\right). \tag{4}$$

Here, r is the internuclear distance given in atomic units. The statistical weights for Σ and Π potentials, d_Σ and d_Π, are 1/3 and 2/3, respectively. In order to calculate P_{CEX}, the long-range form of the potential is adapted

$$V(r)_{g,u} = -\frac{\alpha}{2r^4} \pm \frac{A}{2}e^{-ar} \tag{5}$$

where α is the polarizability of the neutral atom and A and a are parameters given in Table II. Then, the exchange energy, ΔV, can be expressed in the exponential form

$$\Delta V(r) = V_g - V_u = Ae^{-ar}. \tag{6}$$

Expressing the exchange energy in the exponential form greatly simplifies the calculation of P_{CEX} as discussed in Section II-D. The fitting parameters given in Table II are obtained by minimizing the 2-norm of the difference between the potential values calculated from (6) and tabulated in [16]

TABLE II
EXPONENTIAL FITTING PARAMETERS FOR EXCHANGE ENERGY.
VALUES ARE GIVEN IN ATOMIC UNITS (1 a.u. = 27.21 eV = 0.529 Å)

Potentials	A	a
$V_{\Sigma g} - V_{\Sigma u}$	6.81	0.69
$V_{\Pi g} - V_{\Pi u}$	-6.53	0.93

Fig. 5.   Classical scattering trajectory.

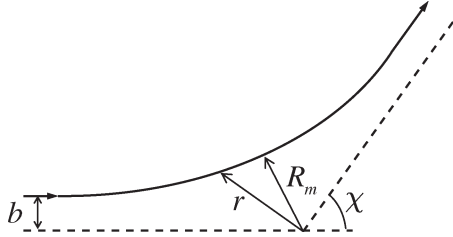Fig. 6.   Deflection functions for classical scattering with spin-orbit free potential for different CM energies.

at internuclear distances greater than 5 a.u., which covers the long range.

C. Deflection Function

Referring to Fig. 5, the center of mass (CM) deflection angle can be calculated by the classical approach [24]

$$\chi(b, E_r) = \pi - 2b \int_{R_m(b,E_r)}^{\infty} \frac{dr}{r^2 \left[1 - b^2/r^2 - V(r)/E_r\right]^{\frac{1}{2}}} \quad (7)$$

where b is the impact parameter, E_r is the initial kinetic energy in the CM frame given as $E_r = (1/2)m_r v_r^2$, m_r is the reduced mass given as $m_r = m_1 m_2/(m_1 + m_2)$, v_r is the relative velocity of the collision pair, and $V(r)$ is the sum of the four spin-orbit free potentials with the statistical weights, $V = 1/6(V_{\Sigma u} + V_{\Sigma g}) + 1/3(V_{\Pi u} + V_{\Pi g})$. Subscripts 1 and 2 denote incident and target particles, respectively. Assuming that the target particle is much slower than the incident particle, the LAB and CM deflection angle and energy are related by the following expression:

$$E = 2E_r \quad (8)$$

$$\theta = \chi/2. \quad (9)$$

The classical turning point or the minimum distance of approach, R_m, is calculated by finding the largest root of the equation

$$1 - b^2/R_m^2 - V(R_m)/E_r = 0. \quad (10)$$

Computing (7) with direct numerical integration can be difficult since the denominator blows up in the limit of $r = R_m$. Instead, (7) is solved by applying Smith's method [25], which uses the Gauss–Mehler formula. At low energies, the deflection function possesses a local minimum value, as shown in Fig. 6, and the differential cross section becomes discontinuous at the angle corresponding to this minimum (i.e., rainbow singularity). Also, the deflection function becomes discontinuous at the
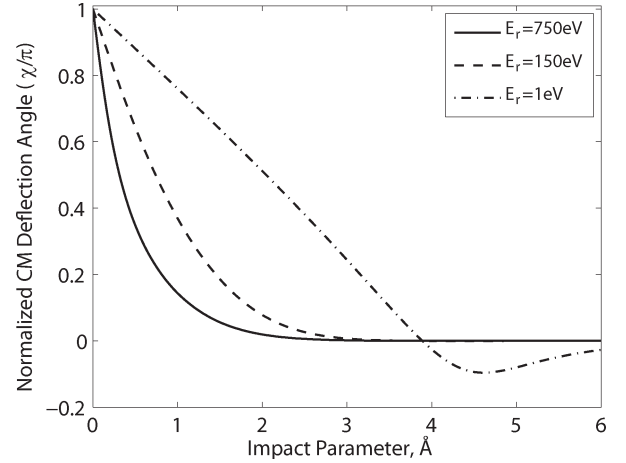
critical angle at even lower energies (i.e., orbiting singularity). These singularities are not realistic, and quantum scattering has to be considered [20], [24]. However, at high energies, the deflection is mostly affected by the repulsive part of the potential at long range so that the deflection function barely has a minimum. In this regime, the classical scattering model is sufficiently accurate to approximate ion–neutral collision behavior [20]. Instead of using the quantum scattering model for low energies, the VHS model is used [18]. Although the scattering characteristics calculated by the model are not realistic, the simple model allows quick calculations of collision mechanics. In this model, the scattering is determined in the same way as the hard sphere model, while the cross section is determined by the following formula given by Dalgarno et al. [26] instead of using the physical cross section:

$$\sigma_i = \frac{64200}{v_r} \text{ Å}^2. \quad (11)$$

The deflection angle is given as follows:

$$\chi(b, E_r) = 2 \cos^{-1} \frac{b}{b_{\max}(E_r)} \quad (12)$$

where $b_{\max}$ is the maximum impact parameter. Once the deflection angle is calculated for some impact parameter, the postcollision velocity can be calculated. The details of the postcollision velocity calculation are given in Appendix A. In the CEX process, the particles of the collision pair are deflected in the same way as the MEX collision, except that the target particle is now an ion after transferring one or more electrons. Therefore, the CM deflection angle of the newly created CEX ions is simply the angle of the target particle, $\pi - \chi$.

Using the empirically determined differential cross sections, $d\sigma/d\Omega$, for a primary xenon ion energy of 300 eV [17], Scharfe et al. [21] formulated functional forms of the differential cross sections, $d\sigma/d\chi$, for the MEX and CEX collisions. The relationship between χ and b for the energy of 300 eV can be deduced using a cumulative distribution function. The model can easily be extended for the case with the ion energy of 1500 eV once $d\sigma/d\Omega$ at the energy is known. When high energy particles elastically collide with background neutrals, energy
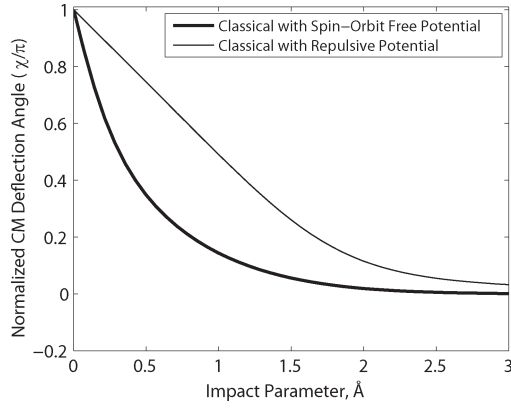
Fig. 7.   Comparison of deflection functions with the spin-orbit free potential and the repulsive part of the potential for ion energy of 1500 eV.

is transfered to the target neutrals, and the incident particle energy is reduced. Therefore, it is necessary to use a model that allows the determination of the deflection angle, not only for the initial primary ion energy but also below this energy level; thus, Scharfe's method cannot be directly applied in the situation of multiple collisions.

Fig. 6 shows the CM deflection angle as a function of the impact parameter with different CM energies. Note that $E_r = 750$ eV corresponds to the primary ion energy ($E = 1500$ eV) used in the ion beam experiment. The deflection function for $E_r = 1$ eV has a small minimum at $b \approx 4.6$ Å, which gives a rainbow singularity at the rainbow angle corresponding to the minimum deflection angle. The CM scattering angle approaches zero as $b \to \infty$; however, it never actually reaches zero. This implies that the total collision cross section is unbounded. In applying the model, it is necessary to provide a cutoff impact parameter or deflection angle [18]. For this computational effort, the cutoff or the maximum impact parameters, $b_{\max}$, are chosen from σ_i for the corresponding incident particle energy. At an ion energy of 1500 eV, $b_{\max}$ is 7.11 Å. As long as the deflection angles at $b > b_{\max}$ are very small, the choice of $b_{\max}$ does not significantly affect the elastic scattering of the particles. In other words, by employing a maximum impact parameter, the deflection angle is artificially set to zero for $b > b_{\max}$, where the deflection angle is very small. It is easy to obtain an idea of what fraction of elastically scattered particles reach the Exit Plate aperture for a single collision condition. Referring to Fig. 1, the angle between the Exit Plate aperture radius and the edge of the beam when entering the Test Cell is $\theta_{cr} = \tan^{-1}\{(2.5 - 1.27)/(153.3 + 6.4)\} = 0.44°$. If the particles experience collisions right at the inlet plane, all the particles deflected with $\theta < \theta_{cr}$ reach the Exit Plate aperture. For the maximum impact parameter chosen in the model, approximately 84% of the particles considered to be experiencing elastic collisions are deflected at $\theta < \theta_{cr}$. Particles can, of course, collide with the background neutrals closer to the Exit Plate aperture than at the inlet plane; therefore, the percentage represents the lower bound. In contrast, if a CEX process takes place, the CEX ions are likely to have very large CM deflection angles when they are created.

Fig. 7 compares $\chi(b, E_r)$ obtained with the classical scattering model with the spin-orbit free potential and the purely re-

pulsive part of the potential ($V_{\Sigma g}$) for an ion energy of 1500 eV. The classical model with the repulsive potential has been applied in a few models [3], [27]. Smaller angle deflections are more likely to take place with the spin-orbit free potential compared to the repulsive potential. At higher energy, the collisions are more affected by the potential at long range, and the spin-orbit free potential is less repulsive at large internuclear distances, giving smaller angle scattering of incident particles.

D. Charge-Exchange Probability

The charge-exchange interaction involves a transition to the other potential, (u) or (g), of the same pair (Σ or Π). Therefore, the charge-exchange probability is calculated from the difference between the elastic scattering phase shifts, $\Delta\eta$ for *gerade* and *ungerade* states ($\Delta\eta = \eta_g - \eta_u$) at a specific impact parameter [7], [17], [19]

$$P_{\text{CEX}}(b) = \sum_l d_l \sin^2 \Delta\eta_l$$

$$= \frac{1}{3} \sin^2 \Delta\eta_\Sigma + \frac{2}{3} \sin^2 \Delta\eta_\Pi. \qquad (13)$$

According to Marchi and Smith, the phase shift difference at large impact parameters can be approximated by [28], [29]

$$\Delta\eta = -\frac{m_r}{\hbar^2 k} \int_{R_m}^{\infty} \frac{\Delta V(r) dr}{[1 - R_m^2/r^2]^{1/2}} \qquad (14)$$

where $\hbar$ is the reduced Planck's constant and k is the wavenumber calculated by $k = \sqrt{2 m_r E_r}/\hbar$. For the case in which the exchange energy is expressed in the exponential form, (14) is solved analytically to give [28], [30]

$$\Delta\eta = \frac{A m_r}{k \hbar^2} b K_1(ab) \qquad (15)$$

where K_1 is the first-order Bessel function of the second kind, and A and a are the parameters given in (6) and Table II. The phase shift differences monotonically increase or decrease depending on the sign of A.

Fig. 8 shows the charge-exchange probability for a primary ion energy of 1500 eV. Note that the CEX probability is not shown at $b < 2$ Å since the approximation to the phase shift difference is not valid at small impact parameters. In this region, the CEX probability oscillates rapidly between 0 and 1, and the average value of 0.5 is typically used in computational models, as well as the differential cross-sectional calculation presented hereinafter. The oscillation between 0 and 1 in the CEX probability continues to about 4 Å, and then, its maximum value in the oscillation starts to decrease due to the stronger interaction of Σ potentials.

The CEX cross section can be calculated from P_{CEX} by [17], [19]

$$\sigma_{\text{CEX}} = 2\pi \int_0^{\infty} P_{\text{CEX}}(b) b db. \qquad (16)$$
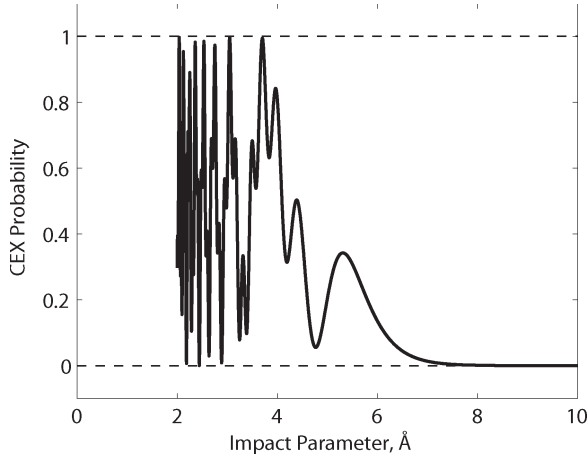
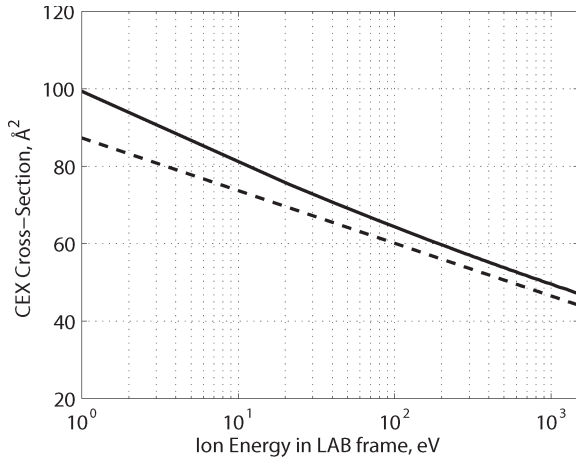Fig. 8. Charge-exchange probability for an ion energy of 1500 eV.

Fig. 9. Charge-exchange cross sections as a function of LAB energy. The solid line is calculated using (17), and the dashed line represents the empirical equation given in (1) [19].

Since the approximation of P_{CEX} at small impact parameters is invalid, the CEX cross section can be rewritten in the following equation, assuming $P_{\text{CEX}} = 0.5$ at $b < b_0$ [30]:

$$\sigma_{\text{CEX}} = 2\pi \int_{b_0}^{\infty} P_{\text{CEX}}(b)b\,db + \frac{\pi}{2}b_0^2. \qquad (17)$$

As shown in Fig. 6, the deflection angles of the projectile particle at $b > 2$ Å are very small ($< 3.4°$) at the energy of 1500 eV. Using $b_0 = 2$ Å, the probability of the CEX interaction occurring in the region of $b > 2$ Å can be calculated by dividing the first term of the right-hand side of (17) by σ_{CEX}, which corresponds to approximately 87%. Since the CM deflection angle of the CEX ions is given as $\pi - \chi$, it is readily seen that the CEX ions are deflected at very large angles in the CM frame ($> 176.6°$) if the collision impact parameter is greater than 2 Å. In contrast, the larger CM deflection angles below 2 Å indicate that some CEX ions are deflected at smaller angles in the CM frame. Fig. 9 shows the CEX cross section as a function of the projectile energy calculated with (1) and (17). The CEX cross section calculated using the spin-orbit

free potential agrees fairly well with the empirical relation. At lower ion energies, the measured cross section is considerably lower than the theoretical cross section. Miller *et al.* noted that the discrepancy was due to the CEX ions at higher energies, exceeding the blocking potential of 1 V, collected in the attenuation experiment. In the computational model described herein, the charge-exchange probability calculated from (13) is used rather than simply assuming $P_{\text{CEX}} = 0.5$. For this reason, it is necessary to use a total ion–neutral collision cross section that covers the largest impact parameter giving $P_{\text{CEX}} > 0$. Using $\sigma_i = 2\sigma_{\text{CEX}}$ neglects the CEX interaction occurring at the impact parameter greater than $\sqrt{2\sigma_{\text{CEX}}/\pi}$. For each energy, the minimum impact parameter, b_{cr}, is found, which satisfies the condition $P_{\text{CEX}} \approx 0$ for $b > b_{cr}$. Then, (2) is obtained by curve fitting the cross sections, πb_{cr}^2, at different energies.

E. Differential Cross Section

Using the scattering angle in the CM frame, the differential cross section can be derived [3]

$$I_{\text{CM}}(\chi, E_r) = \left. \frac{d\sigma(\chi)}{d\Omega} \right|_{CM} = \left| \frac{b}{\sin\chi \left(\frac{d\chi}{db} \right)} \right|. \qquad (18)$$

Here, $d\chi/db$ can be approximated by using first-order difference equations. Taking into account the backscattered CEX ions, the differential cross section can be rewritten as follows [17]:

$$I_{\text{CM}}(\chi) = (1 - P_{\text{CEX}}(\chi))\,I_{\text{CM}}(\chi) + P_{\text{CEX}}I_{\text{CM}}(\pi-\chi). \qquad (19)$$

The first and second terms on the right-hand side of (19) denote the MEX and CEX collision contributions to the total differential cross section, respectively. If the collision partners have equal mass, the CM differential cross sections can be converted into the LAB reference frame by [3]

$$\left. \frac{d\sigma}{d\Omega} \right|_{\text{LAB}} = \left. \frac{d\sigma}{d\Omega} \right|_{\text{CM}} 4\cos(\chi/2). \qquad (20)$$

For the CEX collision, the LAB differential cross section is calculated by replacing χ with $\pi - \chi$ in (20).

Fig. 10 plots the LAB cross sections derived using the classical scattering with the spin-orbit free potential and the repulsive part of the potential $(V_{\Sigma g})$ for an ion energy of 1500 eV. In this figure, $P_{\text{CEX}} = 0.5$ is used for simplicity [7], which is a reasonable assumption except near 0 and 90°. The nonsymmetric behavior of the solutions about 45° is caused by the transformation from the CM to LAB frame. The two differential cross sections have a very similar trend in that both potentials lead to a large probability in small angle scattering. For the repulsive potential, larger differential cross sections at intermediate angles indicate relatively larger scattering as shown in Fig. 7.
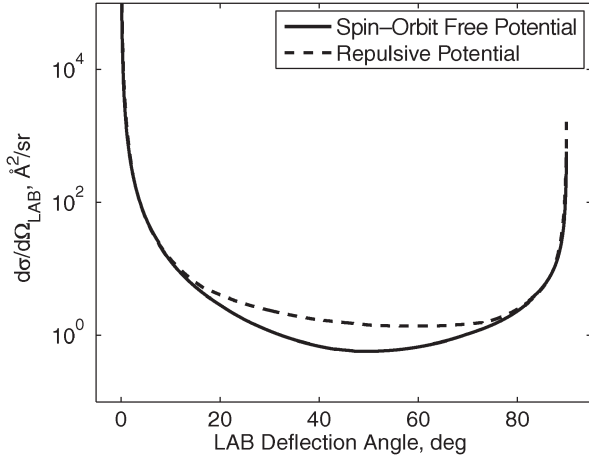
Fig. 10. LAB differential cross sections for an ion energy of 1500 eV calculated using the classical scattering model with the spin-orbit free potential and the purely repulsive part of the interaction potential.

III. ANALYTICAL MODEL FOR DOWNSTREAM CURRENT

A flux Γ' of the beam ions traveling a distance of dx can be expressed in terms of initial flux Γ, neutral density n_o, and the collision cross section σ [31]

$$\Gamma' = \Gamma(1 - n_o \sigma dx). \tag{21}$$

Then, the change of Γ with distance is

$$\frac{\Gamma' - \Gamma}{dx} = \frac{d\Gamma}{dx} = -n_o \sigma \Gamma. \tag{22}$$

Integrating (22), the ion beam current at any distance, x, is calculated

$$J = J_0 \exp(-n_o \sigma x) \tag{23}$$

where J is given as $J = e\Gamma A$. Equation (23) can be used to predict the total current measured at the Collector Plate. If it is assumed that the ions experiencing both MEX and CEX collisions are deflected at large enough angles, then the cross section in (23) is simply $\sigma = \sigma_i$. However, the deflection functions given in Section II predict a very high probability of small angle scattering due to elastic collisions. Therefore, most of the primary ions experiencing MEX collisions are essentially "unscattered" (i.e., they will pass through the Exit Plate aperture in the experiment described in [11] and [12]), and $\sigma = \sigma_{CEX}$ is the appropriate cross section to use in (23). It should be noted that using $\sigma = \sigma_{CEX}$ predicts a slightly larger electrode current than the current due to the primary ions only since there are a small number of primary ions deflected at large angles.

IV. RESULTS AND DISCUSSION

Fig. 11 shows the sum of currents at the Back Aperture and the Collector Plate, predicted by the computational and the analytical models and measured in the ion beam experiment [11], [12]. Note that the current values are normalized with the sum of the currents measured at all the electrodes to clearly show the
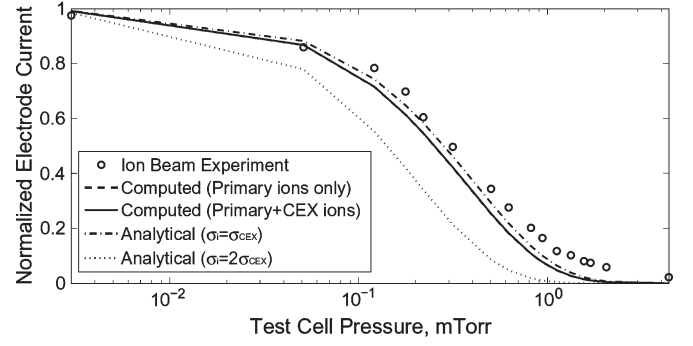

Fig. 11. Normalized electrode current at Back Aperture and Collector Plate. Most of the current to the electrode is due to the primary ions, so the contribution of the CEX ions to the current is negligible.
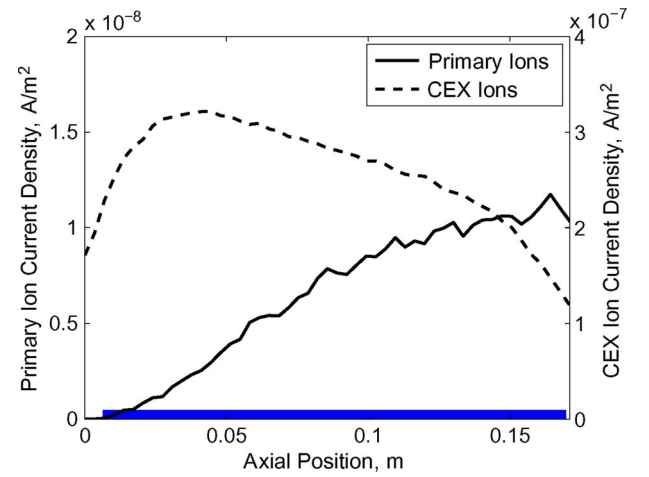

Fig. 12. Ion current density along the radius of the Test Cell at background neutral pressure of 0.22 mtorr. Thick solid line along abscissa axis represents the Inner Cylinder.

trends in collisionality as discussed in [11] and [12]. It can be seen in Fig. 11 that the computational model and the analytical model with $\sigma = \sigma_{CEX}$ agree well with the experimental result. At very low pressure, most of the primary ions go through the Exit Plate orifice. As the pressure is increased, a fraction of the primary ions increasingly diverge from the beam because of the MEX and CEX collisions, and the current reaching the Exit Plate orifice is decreased exponentially as predicted by (23). Although the classical scattering model predicts a very large probability in small angle scattering, the MEX ions can be deflected at relatively larger angles. The analytical model with $\sigma = \sigma_{CEX}$ predicts slightly higher currents going through the Exit Plate orifice than the currents due to the primary ions because using $\sigma = \sigma_{CEX}$ in (23) is equivalent to assuming that all the MEX ions make it through the orifice. It is clearly seen that the analytical model with $\sigma = 2\sigma_{CEX}$ is far off from the other results because it neglects effectively "unscattered" primary ions (the MEX ions with very small deflection angles) in the electrode current.

Figs. 12 and 13 plot the computed ion current density as a function of position along the Inner Cylinder and Exit Plate at the background pressure of 0.22 mtorr, respectively. Based on the collision model used in the simulation, the primary ions are
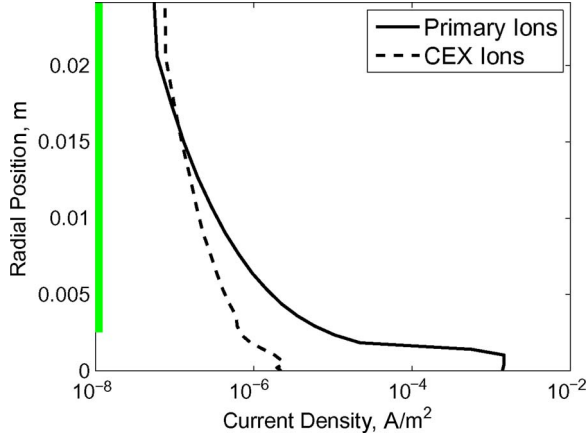
Fig. 13. Ion current density along the downstream end of the Test Cell at background neutral pressure of 0.22 mtorr. Thick solid line along ordinate axis represents the Exit Plate.

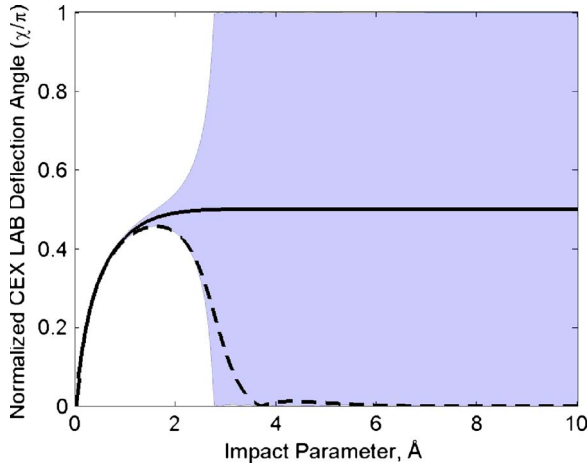Fig. 15. Postcollision CEX ion speed normalized to thermal speed.

Fig. 14. LAB-frame CEX ion deflection angle with respect to direction of incident particle velocity. Shaded area represents possible range of CEX ion deflection angle for collisions with thermal neutrals. Solid and dashed lines represent cases with stationary neutrals and neutrals moving in the same direction as the incident primary ions, respectively.
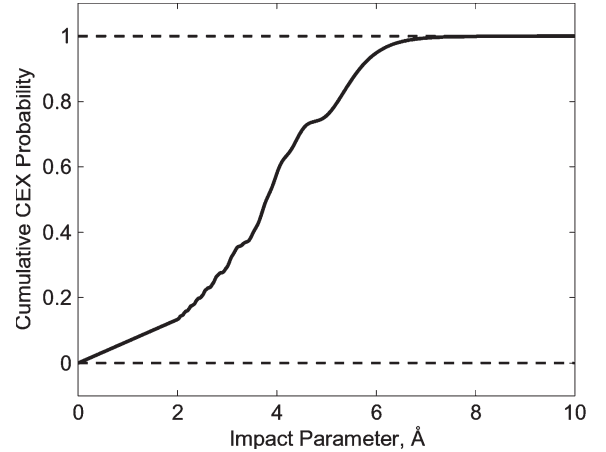
Fig. 16. Cumulative CEX collision probability as a function of impact parameter.

most likely scattered at very small angles. Therefore, the MEX ions infrequently reach the Inner Cylinder, while a significant number of MEX ions can reach the Exit Plate. The CEX ions, in contrast, contribute to the currents on both electrodes. Fig. 14 shows the LAB-frame CEX ion deflection angle with respect to the direction of incident particle velocity for collisions with thermal neutrals. Fig. 14 also plots the deflection angle under the assumptions of stationary neutrals and neutrals moving in the same direction as the incident primary ions; the second assumption is a fair approximation for neutrals in ion thruster plumes. If we assume that the background neutrals are stationary in collision calculations, the majority of the CEX ions are deflected at ∼90° as shown in Fig. 14 and move almost perpendicularly toward the Inner Cylinder. However, in order to find the CEX ion trajectories correctly, it is necessary to incorporate the fact that the neutrals are in random thermal motion. For the case of collisions with thermal neutrals, the CEX ion velocity distribution is close to isotropic for the impact parameter exceeding 3 Å as suggested by the range of the
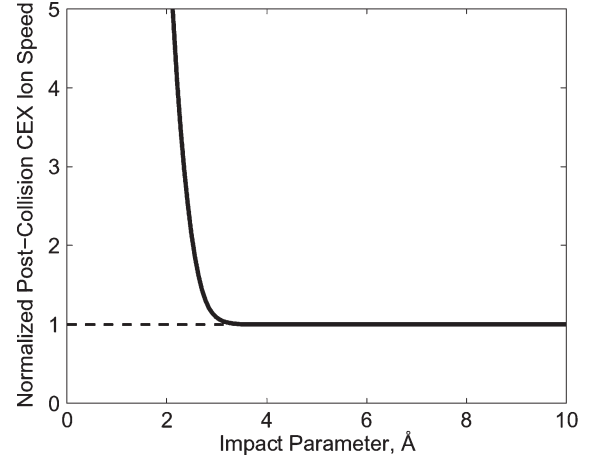
deflection angle (see Fig. 14) and CEX ion speed (see Fig. 15). This corresponds to over 70% of the CEX ions as seen in Fig. 16, and the CEX ion population contributes to the Exit Plate current. The very high CEX ion current at the Inner Cylinder can be explained by the large aspect ratio of the Test Cell. In Fig. 13, the CEX ion current density decreases with increasing radial position. If we take the CEX ions to be initiated along the centerline of the Test Cell with isotropic velocity distribution, then the trend can be explained easily; we can assume that all the CEX ions are created in the beam since the primary ions experience less than one CEX collision on average for the neutral pressure of 0.22 mtorr. The current density at the Exit Plate is proportional to the flux of the CEX ions perpendicular to the surface. Therefore, the current density decreases with increasing radial position as the angles between the axis and the impact position become larger. When the CEX ions are initiated farther downstream but still inside the Test Cell, the change in the angle becomes more dramatic with the radial position. The electric field caused by the space charges in the beam does not significantly affect the shape of the beam itself because of its low ion density ($< 5 \times 10^{11}$ m^{-3}). As shown in Fig. 17, the maximum potential is approximately 0.08 V, which indicates
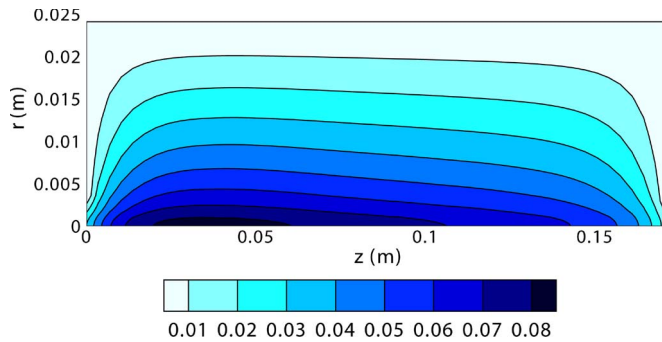
Fig. 17. Contour of potential at background neutral pressure of 0.22 mtorr. The bottom boundary of the contour plot corresponds to the axis of symmetry of the Test Cell.
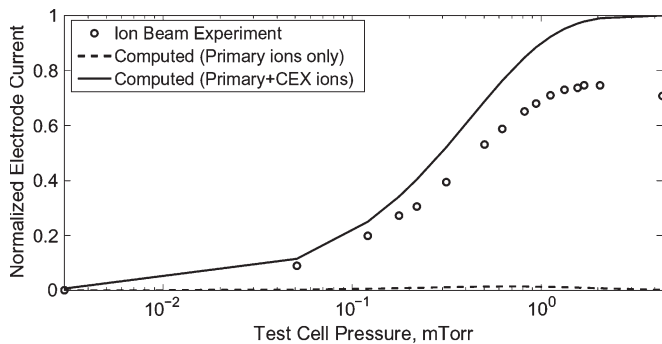

Fig. 18. Normalized electrode current at Inner Cylinder. The currents due to the primary ions are almost negligible.
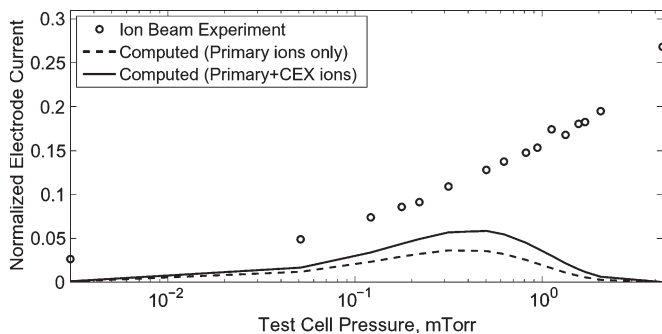

Fig. 19. Normalized electrode current at Exit Plate. Both primary and CEX ions contribute to the computed currents.

that the potential energy is much smaller than the primary ion energy. However, the majority of the CEX ions have energies on the same order of magnitude as the potential energy due to the high probability of large angle scattering in the CM frame. The CEX ions initially heading toward the Exit Plate can be deflected toward the Inner Cylinder due to the radial component of the electric field. Thus, the electric field acts to reduce the CEX ion current at the downstream end of the Test Cell.

Figs. 18 and 19 plot the normalized currents predicted by the computational model and measured during the ion beam experiment at the Inner Cylinder wall and the Exit Plate, respectively. Since the CEX ions are the main contributor to the Inner Cylinder current, the initial increase is primarily due to the rapid rise in the CEX ion population as shown in Fig. 20. As discussed earlier, both primary and CEX ions contribute to the Exit Plate
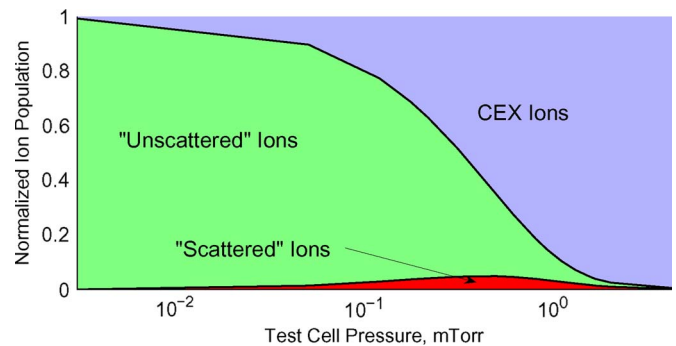

Fig. 20. Types of ions before impacting the electrodes. "Scattered" ions are the MEX ions deflected at large enough angles such that they do not pass through the Exit Plate orifice and do not experience a CEX collision before being collected at the electrodes.

current. In Fig. 18, it can be seen that the computed electrode current agrees fairly well with the experiment up to about 0.2 mtorr. The computational model predicts a higher Inner Cylinder current past the pressure of 0.2 mtorr compared to the measured current during the experiment. Disagreement is also seen in the Exit Plate current. As shown in Fig. 19, the computed Exit Plate current decreases past the pressure of 1 mtorr, whereas the measured Exit Plate current increases steadily. At Test Cell pressures greater than about 0.22 mtorr, the mean free path for elastic (MEX + CEX) collisions is on the order of the length of the Test Cell. Therefore, the difference between the simulation and the experiment becomes significant when a particle experiences multiple collisions before reaching an electrode.

When energetic particles impact solid surfaces, secondary electrons are emitted as a result of electron excitation due to Coulomb interactions with the nuclei and electrons. Secondary electron yield (SEY) is typically larger for greater incident particle energies, and the primary ions as well as the fast neutrals created from the CEX collisions are more responsible for the secondary electron emission compared to the low energy CEX ions and the background neutrals. The SEY for the 1500-eV xenon ion or atom incident to stainless steel is not available. More recent data with the Inner Cylinder wall biased relative to the Exit Plate [32] suggest that the secondary electrons significantly affect currents measured at the electrodes. If the same interaction potential is assumed for atom–atom collisions, a large fraction of the fast neutrals impact the Exit Plate, while a very small fraction are deflected at large enough angles to reach the Inner Cylinder. As shown in Fig. 20, the CEX population increases exponentially with increasing neutral pressure. Since the same number of fast neutrals is created as CEX ions as a result of CEX collision events, the fast neutral population increases exponentially as well. Therefore, the fast neutral current to the Exit Plate increases with increasing Test Cell pressure. As a result, a significant number of electrons are emitted from the Exit Plate, increasing the Exit Plate current as they leave and reducing the Inner Cylinder current as they impact it. Incorporating secondary electron emission from electrodes into the model is currently in development.

In the experiment [11], [12], it is difficult to obtain the exact values for the beam divergence at all the Test Cell

pressures examined. Therefore, a sensitivity study on the beam divergence was conducted to see if the simulation results are improved by inputting some reasonable divergence angles. As long as the beam does not impinge the Exit Plate directly, the simulation results do not change significantly from the case with no beam divergence. Also, the direct impingement of the beam is not likely as seen in the trends in Figs. 11 and 19. In addition, it is found that the beam ion density is so low that the space charges do not affect the beam significantly, and the space charge contributions to the beam divergence are minimal. Therefore, the beam divergence is not the primary source of the discrepancy in the results, compared to the likely secondary electron contributions to the electrode current.

V. CONCLUSION

A PIC-MCC model is implemented to investigate the collisional behavior of heavy plasma species and is compared to the results of a well-characterized simple ion beam experiment [11], [12]. The collision mechanisms implemented in the simulation are the MEX and CEX collisions. The scattering due to the two types of collisions is approximated by the classical scattering model with spin-orbit free potential and the VHS model. Poisson's equation is solved computationally to calculate the electric potential in the computational domain. Primary and CEX ions are tracked separately, and their trajectories are computed. The currents at different electrodes predicted by the simulation are compared with the ion beam experiment results.

The simulation results agree fairly well with the experiment up to the Test Cell pressure of 0.2 mtorr; up to that Test Cell pressure, each primary ion experiences a single collision on average. Multiple collisions occur at higher pressures, and the simulation results start to diverge from the experimental result. The discrepancy is likely due to the secondary electrons created from energetic particles impacting the electrodes as indicated by more recent data provided in [10] and [32]. If the atom–atom interaction potential is similar to that used in the model for ion–atom collisions, an increasing number of fast neutrals should impact the Exit Plate as the Test Cell pressure is increased. Then, most of the secondary electrons ejected from the Exit Plate impact the Inner Cylinder because of the large aspect ratio of the Test Cell, resulting in increased Exit Plate current and decreased Inner Cylinder current. Therefore, the discrepancy between the computational and the experimental results should be reduced as the secondary electrons are incorporated in the model.

In order to incorporate the secondary electrons in the model, the destinations of fast neutrals will be computed using the same scattering model but with a different interaction potential function applicable for atom–atom collisions. One of the candidates for the Xe + Xe potential function is a version of the Hartree–Fock-dispersion potential obtained by Dham et al. [33] The SEY is dependent on several parameters, including incident particle energy, types of incident gas and target material, incident angles, etc. Once the functional form of the SEY as a function of these parameters is found, the secondary electron current ejected from a wall as a result of incident particle flux can be calculated and tracked through the domain.

APPENDIX
DETERMINATION OF POSTCOLLISION VELOCITY

Because of the range of Test Cell pressures varied during the experiment, the gas is dilute enough that each collision can be considered to involve only two particles. During an elastic collision, it is assumed that the net translational energy of the collision pair is conserved. The velocities after the elastic and CEX collisions are calculated using conservation equations for linear momentum and energy

$$\mathbf{v_1^*} = \frac{m_1\mathbf{v_1} + m_2\mathbf{v_2}}{m_1 + m_2} + \frac{m_2}{m_1 + m_2}\mathbf{v_r^*} \tag{24}$$

$$\mathbf{v_2^*} = \frac{m_1\mathbf{v_1} + m_2\mathbf{v_2}}{m_1 + m_2} - \frac{m_1}{m_1 + m_2}\mathbf{v_r^*} \tag{25}$$

where the superscript $*$ denotes postcollision and subscripts 1 and 2 represent incident and target particles, respectively. In the precollision relative velocity, v_r, reference frame (denoted by the $x' - y' - z'$ coordinate), v_r^* can be calculated simply by the following expression, assuming that v_r is aligned with the z'-axis:

$$\mathbf{v_r^*} = v_r \begin{pmatrix} \sin\chi\cos\gamma \\ \sin\chi\sin\gamma \\ \cos\chi \end{pmatrix}^T \begin{pmatrix} \hat{x}' \\ \hat{y}' \\ \hat{z}' \end{pmatrix}. \tag{26}$$

Here, χ is the CM deflection angle and γ is the azimuthal angle. The transformation between the inertial and the precollision relative velocity reference frames can be done by

$$\begin{pmatrix} \hat{x}' \\ \hat{y}' \\ \hat{z}' \end{pmatrix} = \begin{bmatrix} \cos\alpha\cos\beta & \sin\alpha\cos\beta & -\sin\beta \\ -\sin\alpha & \cos\alpha & 0 \\ \cos\alpha\sin\beta & \sin\alpha\sin\beta & \cos\beta \end{bmatrix} \begin{pmatrix} \hat{x} \\ \hat{y} \\ \hat{z} \end{pmatrix} \tag{27}$$

where α and β are the angles between the two reference frames given by

$$\sin\alpha = v_{ry}/\sqrt{v_{rx}^2 + v_{ry}^2} \quad \cos\alpha = v_{rx}/\sqrt{v_{rx}^2 + v_{ry}^2}$$

$$\sin\beta = \sqrt{v_{rx}^2 + v_{ry}^2}/v_r \quad \cos\beta = v_{rz}/v_r. \tag{28}$$

Given the precollision velocities of both incident and target particles, the postcollision velocities of the two particles can be calculated using (24)–(28) once χ and γ are determined. Because any value for γ is equally probable, γ is chosen simply by $\gamma = 2\pi(\text{rand}\#)$. Similarly, b is determined with the random number generator, $b = b_{\max}\sqrt{\text{rand}\#}$, and the corresponding value for χ is calculated from the deflection function described in Section II-C.

REFERENCES

[1] R. G. Jahn, *Physics of Electric Propulsion*. New York, NY, USA: Dover, 2006.

[2] R. A. Dressler and Y.-H. Chiu, "Quantifying plasma collision processes in xenon powered electric propulsion systems," in *Proc. AIP Conf. 27th Int. Symp. Rarefied Gas Dyn.*, 2011, pp. 1065–1072.

[3] I. Mikellides, I. Katz, R. Kuharski, and M. Mandell, "Elastic scattering of ions in electrostatic thruster plumes," *J. Propul. Power*, vol. 21, no. 1, pp. 111–118, Jan./Feb. 2005.

[4] J. Brophy, I. Katz, J. E. Polk, and J. R. Anderson, "Numerical simulations of ion thruster accelerator grid erosion," presented at the Proc. 38th Joint Propul. Conf., Indianapolis, IN, USA, 2002, AIAA-2002-4261.

[5] R. E. Wirz, J. R. Anderson, D. M. Goebel, and I. Katz, "Decel grid effects on ion thruster grid erosion," *IEEE Trans. Plasma Sci.*, vol. 36, no. 5, pp. 2122–2129, Oct. 2008.

[6] J. R. Anderson, I. Katz, and D. Goebel, "Numerical simulation of two-grid ion optics using a 3D code," presented at the Proc. 40th AIAA Joint Propul. Conf., Fort Lauderdale, FL, USA, 2004, AIAA-2004-3782.

[7] I. D. Boyd and R. A. Dressler, "Far field modeling of the plasma plume of a Hall thruster," *J. Appl. Phys.*, vol. 92, no. 4, pp. 1764–1774, Aug. 2002.

[8] D. Oh, "Computational Modeling of Expanding Plasma Plumes in Space Using a PIC-DSMC Algorithm," Ph.D. dissertation, MIT, Cambridge, MA, USA, 1997.

[9] P. N. Giuliano and I. D. Boyd, "Effects of detailed charge exchange interactions in DSMC-PIC simulation of a simplified plasma test cell," presented at the Proc. 32nd Int. Elect. Propul. Conf., Wiesbaden, Germany, 2011, IEPC-2011-112.

[10] P. N. Giuliano and I. D. Boyd, "Analysis of a plasma test cell including non-neutrality and complex collision mechanisms," presented at the Proc. 48th AIAA Joint Propul. Conf., Atlanta, GA, USA, 2012, AIAA-2012-3316.

[11] R. E. Wirz, L. Chu, M. Patino, H.-S. Mao, and S. J. Araki, "Well-characterized plasma experiments for validation of computational models," presented at the Proc. 32nd Int. Elect. Propul. Conf., Wiesbaden, Germany, 2011, IEPC-2011-122.

[12] R. E. Wirz, M. Patino, L. Chu, H.-S. Mao, and S. J. Araki, "Simple plasma experiments for investigation of plasma behavior and model validation," *Plasma Sources Sci. Technol.*, submitted 2013.

[13] W. G. Vincenti and C. H. Kruger, *Introduction to Physical Gas Dynamics*. Melbourne, FL, USA: Krieger, 1965.

[14] C. K. Birdsall and A. B. Langdon, *Plasma Physics via Computer Simulation*. New York, NY, USA: McGraw-Hill, 1991.

[15] W. Ruyten, "Density-conserving shape factors for particle simulations in cylindrical and spherical coordinates," *J. Comput. Phys.*, vol. 105, no. 2, pp. 224–232, 1993.

[16] I. Paidarova, "Accurate ab initio calculation of potential energy curves and transition dipole moments of the Xe_2 molecular ion," *Chem. Phys.*, vol. 274, no. 1, pp. 1–9, Dec. 2001.

[17] Y.-H. Chiu, R. A. Dressler, D. J. Levandier, C. Houchins, and C. Y. Ng, "Large-angle xenon ion scattering in Xe-propelled electrostatic thrusters: Differential cross sections," *J. Phys. D: Appl. Phys.*, vol. 41, no. 16, p. 165 503, Aug. 2008.

[18] G. A. Bird, *Molecular Gas Dynamics and the Direct Simulation of Gas Flows*. Oxford, U.K.: Clarendon, 1994.

[19] J. S. Miller, S. H. Pullins, D. J. Levandier, Y.-H. Chiu, and R. A. Dressler, "Xenon charge exchange cross sections for electrostatic thruster models," *J. Appl. Phys.*, vol. 91, no. 3, pp. 984–991, Feb. 2002.

[20] I. Katz, G. Jongeward, V. Davis, M. Mandell, I. Mikellides, I. Boyd, A. Arbor, K. Kannenberg, and D. King, "A Hall effect thruster plume model including large-angle elastic scattering," presented at the Proc. 37th AIAA/ASME/SAE/ASEE Joint Propul. Conf. Exhib., Salt Lake City, UT, USA, 2001, AIAA-2001-3355.

[21] M. K. Scharfe, J. Koo, and G. Azarnia, "DSMC implementation of experimentally-based Xe^+ + Xe differential cross sections for electric propulsion modeling," in *Proc. AIP Conf. 27th Int. Symp. Rarefied Gas Dyn.*, 2011, vol. 298, pp. 1085–1090.

[22] M. Amarouche, G. Durand, and J. P. Malrieu, "Structure and stability of Xe_n^+ clusters," *J. Chem. Phys.*, vol. 88, no. 2, pp. 1010–1018, Jan. 1988.

[23] J. A. S. Barata and C. A. N. Conde, "Calculation of drift velocities and diffusion coefficients of Xe^+ ions in gaseous xenon," *IEEE Trans. Nucl. Sci.*, vol. 52, no. 6, pp. 2889–2894, Dec. 2005.

[24] M. S. Child, *Molecular Collision Theory*. London, U.K.: Academic, 1974.

[25] F. J. Smith, "The numerical evaluation of the classical angle of deflection and of the J.W.K.B. phase shift," *Physica*, vol. 30, no. 3, pp. 497–504, Mar. 1964.

[26] A. Dalgarno, M. R. C. McDowell, and A. Williams, "The mobilities of ions in unlike gases," *Proc. R. Soc. Lond. A, Math. Phys. Sci.*, vol. 250, no. 982, pp. 411–425, Apr. 1958.

[27] S. J. Araki and R. E. Wirz, "Collision modeling for high velocity ions in a quiescent gas," presented at the Proc. 42nd AIAA Plasmadyn. Lasers Conf., Honolulu, HI, USA, 2011, AIAA-2011-3740.

[28] R. P. Marchi and F. T. Smith, "Theory of elastic differential scattering in low-energy He^+ + He collisions," *Phys. Rev.*, vol. 139, no. 4A, pp. 1025–1038, Aug. 1965.

[29] F. J. Smith, "Oscillations in the caesium and rubidium resonant charge transfer cross sections," *Phys. Lett.*, vol. 20, no. 3, pp. 271–271, Feb. 1966.

[30] S. H. Pullins, R. A. Dressler, R. Torrents, and D. Gerlich, "Guided-ion beam measurements of Ar^+ + Ar symmetric charge-transfer cross sections at ion energies ranging from 0. 2 to 300 eV," *Z. Phys. Chem.*, vol. 214, no. 9, pp. 1279–1297, Sep. 2000.

[31] F. F. Chen, *Introduction to Plasma Physics and Controlled Fusion Volume 1: Plasma Physics*, 1st ed. New York, NY, USA: Springer-Verlag, 2006.

[32] M. I. Patino, L. E. Chu, and R. E. Wirz, "Ion-neutral collision analysis for a well-characterized plasma experiment," presented at the Proc. 48th AIAA Joint Propul. Conf., Atlanta, GA, USA, 2012, AIAA-2012-4119.

[33] A. K. Dham, W. J. Meath, A. R. Allnatt, R. A. Aziz, and M. J. Slaman, "XC and HFD-B potential energy curves for Xe-Xe and related physical properties," *Chem. Phys.*, vol. 142, no. 2, pp. 173–189, Apr. 1990.

Samuel J. Araki received B.S. and M.S. degrees in aerospace engineering from the University of California, Los Angeles, CA, USA, in 2007 and 2009, respectively, where he is currently working toward a Ph.D. degree.

His doctoral research includes heavy species modeling and the development of a particle-in-cell model to investigate near-surface cusp confinement of microscale plasma discharges for microthrusters and terrestrial plasma sources.

Richard E. Wirz received a B.S. degree in aerospace engineering and a B.S. degree in ocean engineering from Virginia Polytechnic Institute and State University (Virginia Tech), Blacksburg, VA, USA, in 1992 and 1993, respectively, and M.S. and Ph.D. degrees in aeronautics and applied sciences from the California Institute of Technology (Caltech), Pasadena, CA, USA, in 2001 and 2005, respectively.

From 2005 to 2009, he was a Senior Engineer with the Electric Propulsion Group, Jet Propulsion Laboratory, Pasadena, CA, USA, specializing in modeling, experimental testing, and mission integration of electric thrusters. He is currently an Assistant Professor with the Department of Mechanical and Aerospace Engineering, University of California, Los Angeles, CA, USA. He designed and developed the world's first noble gas miniature ion thruster and is a recognized expert in miniature and precision plasma thruster design and development, plasma modeling for electric thrusters, and advanced propulsion concepts. His current research interests include electric and micropropulsion, low-temperature plasma and plasma discharges, spacecraft and space mission design, and alternative energy generation and storage.